Title

Almond shell nanocellulose: Characterization and self-assembling into fibers, films, and aerogels

Authors

Fukuda, Juri
Hsieh, You-Lo

Publication Date

2022-10-01

DOI

10.1016/j.indcrop.2022.115188

Industrial Crops & Products 186 (2022) 115188

Contents lists available at ScienceDirect

Industrial Crops & Products

journal homepage: www.elsevier.com/locate/indcrop

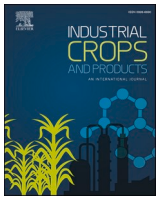

Almond shell nanocellulose: Characterization and self-assembling into fibers, films, and aerogels

Juri Fukuda, You-Lo Hsieh *

Biological and Agricultural Engineering Department, University of California at Davis, Davis, CA 95616-8722, United States

ARTICLE INFO

Keywords:
Nanocellulose
Amphiphilicity
Interface
Aerogel
Fiber
Film

ABSTRACT

Cellulose has been efficiently isolated from almond shell (AS) of a soft-shell Carmel variety by a two-step $NaClO_2$ oxidation-KOH alkali protocol at over 35 % yield, then optimally TEMPO-oxidized and blended to yield 92 % and averagely 1.2 nm high (H), 5.2 nm wide (W), and 1.4 μm long (L) cellulose nanofibers (CNFs) with 58.6 % crystallinity and 1.3 mmole/g charge. With uniquely high 1167 L/H aspect ratio and 4.3 W/H lateral anisotropy, AS CNFs self-assembled into 1D fibers and 3D aerogels by freezing at − 196 °C and − 20 °C, respectively, then lyophilization as well as 2D films by air drying. All fibers were fully re-dispersable in water to individualized CNFs whereas aerogels were amphiphilic super-absorbents, absorbing slightly more hydrophobic chloroform than water, and films were hydrophilic on the surfaces and absorbed ca. three times more water than decane. The fully aqueous dispersible fibers, amphiphilic and water resilient aerogels, and organic resilient films are attributed to the interfacial associations of AS CNF driven by their uniquely high aspect ratio and cross-sectional anisotropy, demonstrating processing potential into versatile 1D to 3D materials.

1. Introduction

Almonds are the largest tree nut crop in the world of which ca. 80 % is produced in California in the U.S. (International Treenuts and Dried Fruits Council, 2020, 2021; Almond Board of California, 2020). In the production of kernels, the almond farming and processing industries generate significant by-products, of which 53.5 % is woody biomass that includes pruning, trees, and shells (19.7 %), and 46.5 % is fleshy biomass with essentially all hulls (Huang and Lapsley, 2019). With shells in near equal mass and hulls twice as the kernels, almond processing alone has generated about three times of biomass of the 1.5 million metric tons of kernels (Huang and Lapsley, 2019). The high lignocellulosic contents of almond woody biomass have been studied to generate energy by thermal conversion (García et al., 2017) and as bioethanol (Gong et al., 2011; Kacem et al., 2016) as well as to produce biochar and activated carbon (Izquierdo et al., 2011; Klasson et al., 2015; Martínez de Yuso et al., 2014; Nabais et al., 2011; Thomas Klasson et al., 2010). Almond shell (AS) has been used directly as a low-cost absorbent for removing cationic dye (Hashemian, 2014), cations/anions (Estevinho et al., 2006; Hashemian, 2014; Maaloul et al., 2017a; Rashid et al., 2022), and pentachlorophenol (PCP) pollutant (Estevinho et al., 2006), or treated with NaOH for removing lead and cadmium ions (Mehrasbi et al., 2009). AS particles have also been studied as fillers to improve the flexural strength and Young's modulus of polypropylene (Chiou et al., 2015; El Mechtali et al., 2015) and polymethyl methacrylate (Sabbatini et al., 2017) composites, where the reinforcement were further enhanced by reduced granule size (Sabbatini et al., 2017), torrefaction (Chiou et al., 2016, 2015), and NaOH treatment (El Mechtali et al., 2015). Recently, AS was applied as a catalyst to mediate a three-component tandem reaction to produce antimicrobial, antiviral, and anticancer drugs (Kamali-Gharamaleki et al., 2021).

The compositions of AS have been determined for the purposes of animal feed (Saura-Calixto et al., 1983), gasification (De Bari et al., 2000), energy production (González et al., 2005; Martínez et al., 1997), xylo-oligosaccharide purification for food and pharmaceutical industry (Nabarlatz et al., 2007), particle board manufacturing (Pirayesh and Khazaeian, 2012), bio-sorbents (Maaloul et al., 2017a), and biomass conversion (Queirós et al., 2020) by various methods, including ASTM (De Bari et al., 2000; Maaloul et al., 2017a; Martínez et al., 1997; Nabarlatz et al., 2007), TAPPI (Maaloul et al., 2017a; Pirayesh and Khazaeian, 2012), Van Soest (González et al., 2005; Saura-Calixto et al., 1983) (Table 1). Overall, AS comprises of 28.9 ± 3.2 % cellulose, 32.1 ± 4.0 % hemicellulose, 29.3 ± 2.2 % lignin, and 3.7–11.8 % organic extractables. Among the three nearly equal lignocellulosic constituents,

* Corresponding author.
E-mail address: ylhsieh@ucdavis.edu (Y.-L. Hsieh).

https://doi.org/10.1016/j.indcrop.2022.115188
Received 15 April 2022; Received in revised form 23 May 2022; Accepted 5 June 2022

cellulose is the most chemically homogenous and has the highest potential as value-added materials and products.

Cellulose is also the only semi-crystalline component of the three. The isolated crystalline domains, i.e., cellulose crystals (CNCs) and nanofibrils (CNFs), have drawn extensive interest because of their outstanding intrinsic tensile strength and Young's modulus, i.e., 7.5 GPa (Wu et al., 2014) and 150 GPa (Iwamoto et al., 2009) for CNCs and 233 MPa (Fukuzumi et al., 2009) and 145 GPa (Iwamoto et al., 2009) for CNFs, respectively. The rod-shaped CNCs are highly crystalline (< 90%) but typically lower in yields (< 30%) whereas the thinner and longer CNFs can reach nearly full yields when isolated by mechanical forces aided by chemical pretreatments but less crystalline (Jiang and Hsieh, 2013). To date, only CNCs have been derived from AS and studied as absorbents for Cu (II) (Maaloul et al., 2017b; Rashid et al., 2022) and Pb (II) (Rashid et al., 2022), and nanopaper (Urruzola et al., 2014) that had shown to be stronger than those from canola straw (Yousefi et al., 2013).

To discover the highest value-added potential of AS toward advanced performance materials, this study aimed at comprehensive investigations of cellulose isolation, cellulose nanofibril (CNF) generation, characterization, and structural formation into one-dimensional (1D), two dimensional (2D), and three-dimensional (3D) materials. The isolation of AS cellulose was evaluated by adopting the 3-step protocol of toluene/ethanol extraction, $NaClO_2$ oxidation, and KOH treatment for rice straw (Jiang and Hsieh, 2013; Lu and Hsieh, 2012), eliminating the oraganic extraction that was effective for sugarcane bagasse (Messa et al., 2021), and reversing the alkaline (KOH or NaOH)-oxidation ($NaClO_2$) process (Rashid et al., 2022; Sun et al., 2004) to compare the yields and purities of cellulose by FTIR and TGA. The 2,2,6,6,-tetramethylpiperidine-1-oxyl (TEMPO) mediated oxidation, first applied to cellulose by Isogai and co-workers (Saito et al., 2007) and optimized to generate CNFs from rice straw cellulose (Jiang et al., 2013), was adopted for producing AS-CNF. The morphology, charge density, and surface chemistry of AS-CNF were characterized by atomic force and transmission electron microscopy, conductometric titration, and solution state proton nuclear magnetic resonance spectroscopy, respectively. Aqueous CNF dispersions were self-assembled into 1D fibers, 2D films, and 3D aerogels under different drying conditions. The structures and re-dispersing behaviors of these fibers, film, and aerogel were analyzed to elucidate CNF surface and interfacial properties critical to their processing, structural formation, and potential applications.

2. Materials and methods

2.1. Materials

Almond shell (AS) was from a soft-shell Carmel variety, harvested and collected in northern California. Toluene (certified), ethanol (EtOH, anhydrous, denatured, Millipore Sigma), sodium chlorite ($NaClO_2$, 80 %, Fluka), acetic acid glacial (CH_3COOH, 99.7 % ACS GR, EMD), potassium hydroxide (KOH, 85 %, EM Science) and sodium hydroxide (NaOH, pellets, 97 %, Millipore sigma) for separation of lignin, hemicellulose and cellulose from AS, sodium hydroxide (NaOH, 1 N, Certified, Fisher Scientific), sodium hypochlorite (NaClO, 11.9 %, reagent grade, Sigma–Aldrich), TEMPO (99.9%, Sigma–Aldrich), sodium bromide (NaBr, BioXtra, 99.6%, Sigma–Aldrich) for oxidation of cellulose, and hydrochloric acid (HCl, 1 N, Certified, Fisher Scientific), acetone (certified), decane (certified), dimethylacetamide (DMAc, certified), deuterium oxide (99.9 atom % D, Millipore sigma) for characterizations of CNFs, were all used as received without further purification. All water used was purified by Milli-Q plus water purification system (Millipore Corporate, Billerica, MA).

2.2. Isolation of AS cellulose

AS was milled (Thomas-Wiley Laboratory Mill model 4, Thomas Scientific, USA) to pass through a 60-mesh sieve (250 μm), then extracted by three different routes. Route 1 followed a previously reported process for rice straw (Lu and Hsieh, 2012) in which ground and sieved AS (30 g) was refluxed with 2:1(v/v) toluene-ethanol in a soxhlet apparatus for 20 h and dried under hood for two days then at 55 °C for another two days. The organic extracted AS was then delignified in acidified sodium chlorite (1.4 % $NaClO_2$, glacial acetic acid (pH 3.5), 1000 mL) at 70 °C for 5 h, and rinsed with water until the filtrate reached neutral. The delignified AS was then treated in 600 mL 5% KOH at room temperature for 24 h then at 90 °C for 2 h, cooled, and vacuum-filtered, then rinsed with copious amount of water until the filtrate became pH neutral. Route 2 was the same as Route 1 except without organic extraction. Route 3 reversed the alkaline treatment with either 5% KOH or NaOH then de-lignification. The wet solid from each extraction step was redispersed in water and frozen in liquid nitrogen (−196 °C) and freeze-dried (FreeZone 1.0 L Benchtop Freeze Dry System, Labconco, Kansas City, MO) and weighed to calculate the yield based on the original mass of AS. Cellulose from the respective Route 1,

Table 1
Almond shell compositions (wt%) reported in the literature.

Species specified in genus *Prunus* (*P.*)	Organic extract	Lignin	Hemi-cellulose	Cellulose	Method	Reference for Method
P. amygdalus (Martínez et al., 1997)	3.7 ± 1.1[a]	27.2 ± 2.0	34.0 ± 4.9	29.3 ± 7.9	ASTM: D-1111[a]; D-1107[b]; D-1106[c], HPLC for carbohydrates	De Bari et al., 2000; Martínez et al., 1997; Nabarlatz et al., 2007
P. dulcis (Maaloul et al., 2017a)	11.8	30.1	25.1	29.9	ASTM: D-1107[b] TAPPI: T222-om[d]; T19m-54[e]	Maaloul et al. 2017a
P. amygdalus var. *sativa* (L.) Focke[f] (Pirayesh and Khazaeian, 2012)	N/A	32.7	35.2	29.1	TAPPI: T222-om[d]	Pyrayesh and Khazaeian, 2012
P. amygdalus (Saura-Calixto et al., 1983)	3.9	27.8 ± 0.1	33.6 ± 6.3	32.6 ± 2.1	Van Soest[g]	Gonzales et al. 2005;Saura-Calixto et al. (1983)
P. dulcis (Mill) D.A. Webb[f] (Queirós et al., 2020)	5.7	28.8	32.4	23.8	Dichloromethane/Ethanol/Water/Acid hydrolysis (72 % and 3–4 % H_2SO_4)	Queirós et al. (2020)

[a] Also 7.4% hot water extractive prior to organic extraction.
[b] Ethanol-toluene extraction to remove catechol, tannins, resin, fats, wax and oil.
[c] Lignin removal in 72% H_2SO_4 at 20 °C for 2 h, then 3% H_2SO_4 at boil for 4 h.
[d] Lignin removal in 72% H_2SO_4 at 20 °C for 2 h, then 3% H_2SO_4 at boil for 4 h.
[e] Holocellulose and cellulose contents were obtained by removing lignin by sodium hypochlorite at 70 °C and hemicellulose from the holocellulose fraction by 10 w/v% NaOH extraction, respectively. Hemicellulose content was determined by the difference between holocellulose and cellulose contents (Nepomuceno et al., 2017).
[f] *Prunus amygdalus* var. *sativa* (L.) Focke is a synonym of *Prunus dulcis* (Mill.) D.A.Webb
[g] Hemicellulose content was the mass difference between Neutral Detergent Fiber (cellulose, hemicellulose, lignin) and acid detergent fiber (cellulose, lignin). Cellulose content was obtained from removing lignin by $KMNO_4$ oxidation whereas lignin content was by dissolving cellulose in 72% H_2S0_4.

2, and 3 was designated as Cell 1, 2, and 3. Herein, all mass was in weight % and noted as % unless specified otherwise.

2.3. TEMPO-oxidized cellulose nanofibrils (CNF)

AS cellulose was TEMPO-oxidized and disintegrated by high-speed blending into CNFs following the procedures for rice straw cellulose (Jiang and Hsieh, 2013). AS cellulose (1.0 g) was magnetically stirred in 100 mL water and combined with 2 mL aqueous mixture of catalytic amount of TEMPO (16.0 mg) and NaBr (100 mg) to which 5 mmol NaClO was added dropwise with pH adjusted to 10 ~ 10.5 using 0.5 N NaOH. The reaction proceeded until the pH ceased to decrease for 15 min and the reaction time recorded. The reaction mixture was neutralized to pH 7 by 0.5 N HCl, then centrifuged (5000 rpm, 15 min) to collect TEMPO-oxidized cellulose precipitate to be dialyzed against water for several days to remove free ions. The dialyzed suspension was diluted to 250 mL to be mechanically blended (Vitamix 5200) at 30,000 rpm for 30 min (15 min x 2), centrifuged (5000 rpm, 15 min) to collect the TEMPO-oxidized CNF-containing supernatant. The CNF yields were calculated gravimetrically from dry mass in triplicate and averaged. All aqueous CNF suspensions were stored at 4 °C before characterization and use.

2.4. Characterization of CNFs

For conductometric titration, 50 μL of 1 N HCl was added to 50 mL of 0.1 wt% CNF suspension to protonate all the carboxyl groups, then titrated with 0.01 M NaOH solution using an OAKTON pH/Con 510 series meter. The surface charge (σ, mmol /g of cellulose) was determined as

$$\sigma = \frac{cv}{m} = \frac{c(v2 - v1)}{m} \quad (1)$$

where c is the NaOH concentration (M), m is the CNF mass (g) in the suspension, and v1 and v2 are NaOH volumes (mL) used from neutralizing the added HCl and carboxylic acid on the CNFs, respectively. Solution state ^{1}HNMR of CNFs was analyzed in D_2O using a Bruker AVIII 800 MHz ^{1}HNMR spectrometer following the procedure for rice straw CNFs (Jiang et al., 2014). CNF dispersion (5 mL at 0.3 %) was precipitated by adding 10 mL acetone then centrifuged (5000 rpm, 15 min) to decant the supernatant which was repeated three times. A fraction of CNF acetone gel was added by 1 mL D_2O, sonicated for 3 min (Branson 2510), then vacuum dried at 60 °C for 1 h and replenished D_2O several times to remove residual acetone to a final ca. 0.2 % CNF concentration. CNFs (0.0005 w/w%, 10 μL) were deposited on mica (highest grade V1 mica discs, 15 mm, Ted Pella, Inc.) and allowed to dry, then scanned under ambient condition using an Asylum Research MFP-3D atomic force microscope (AFM, Santa Barbara, CA) in tapping mode with OMCL-AC160TS standard silicon probes (tip radius < 10 nm, spring constant = 28.98 N/m, resonant frequency = ~310 kHz, Olympus Corp.) at a 1 Hz scan rate and 512 pixels × 512 pixels image resolution. The height (H) of CNFs in AFM images was processed with Igor Pro 6.21. Width (W) and length (L) of ODE-CNFs were imaged at 40-kV accelerating voltage by Philip CM12 transmission electron microscope (TEM). A drop of 10 μL CNF (0.0005, w/w%) was deposited onto glow-discharged carbon-coated TEM grids (300-mesh copper, formvar-carbon, Ted Pella Inc., CA) and air-dried, negatively stained with 2 % uranyl acetate solution for 30 s, then the excess blotted with a filter paper to dry at ambient condition. Over 200, 100, and 50 of respective H, W, and L measurements from several AFM and TEM images were used to obtain the mean and standard deviation.

2.5. Fibers, aerogels, and films

Fibers were self-assembled by freezing aqueous CNFs (0.01, 0.05, 0.1, 0.3 w/v%) in polypropylene tubes in liquid nitrogen (−196 °C, 15 min), then lyophilized (−50 °C, 0.05 mbar, 2 d) in a freeze-drier (FreeZone 1.0 L Benchtop Freeze Dry System, Labconco, Kansas City, MO). Aerogels were fabricated by freezing aqueous CNFs (0.05, 0.1, 0.3, 0.6 w/v%) in polypropylene tubes at − 20 °C for 12 h (ThermoFisher, IsoTemp, Model HF-5017), and lyophilized. Films were casted from aqueous CNFs (98.6 g), 0.3%, mechanically stirred for 1 h and ambiently dried (24 h) in hexagonally shaped polystyrene (PS) weighing tray into 51.4 cm^2 area.

2.6. Characterization of CNF fibers, films, aerogels

Fourier transform infrared spectroscopy (FTIR) spectra were collected of samples in KBr (1:50, w/w) disks using a Thermo Nicolet 6700 spectrometer (Thermo Fisher Scientific, USA) in the transmittance mode from 4000 to 400 cm^{-1} at a 4 cm^{-1} resolution and 128 scans. X-ray diffraction (XRD) spectra of freeze-dried cellulose 2 and CNF2, compressed between two glass slides into ca. 1 mm thick, was collected from 5° to 40° at a scan rate of 2° per m on a Scintag XDS 2000 powder diffractometer using a Ni-filtered Cu Kα radiation ($\lambda = 1.5406\ \AA$) at 45 k V anode voltage and 40 mA current. Crystallinity index (*CrI*) was calculated by the 200 peak (I_{200}, $2\theta = 22.6°$) intensity and the minimum between the 200 and 110 peaks (I_{am}, $2\theta = 18.7°$) using Segal equation (Segal et al., 1959)

$$\mathrm{CrI} = \frac{I_{200} - I_{am}}{I_{200}} \mathrm{x}100 \quad (2)$$

The crystallite dimensions were calculated using Scherrer equation (Scherrer, 1918)

$$\mathrm{D_{hkl}} = \frac{0.9 \quad \lambda}{\beta 1/2 \quad cos \quad \theta} \quad (3)$$

where D_{hkl} is the crystallite dimension in the direction normal to the *h k l* lattice planes, λ is the X-ray radiation wavelength (1.5406 Å). $\beta_{1/2}$ is the width at half-maximum of the diffraction peak, and θ is the corresponding Bragg angle. $\beta_{1/2}$ was determined by multiple peak fitting in Origin software. The fiber and aerogel morphologies were imaged by a field emission scanning electron microscope (FE-SEM) (XL 30-SFEG, FEI/Philips, USA) at 5-kV accelerating voltage. Each sample was adhered to aluminum stub covered with conductive carbon tape and sputter coated with gold at 20 mA for 2 min (Bio-Rad SEM coating system). Fiber widths were measured from more than 100 individual fibers by using ImageJ software. The aerogel density (ρ_a) was calculated from the mass and volume of 1 cm cylindrical section, and the porosity (ϕ, %) was calculated as:

$$\mathrm{Porosity}\ (\phi) = \left(1 - \frac{\rho_a}{\rho_c}\right) \mathrm{x}\ 100\% \quad (4)$$

where ρ_c is the specific density of cellulose (1.6 g/cm^3).

Liquid absorption (mL/g) was calculated as:

$$\mathrm{Absorption} = \frac{\frac{(w_s - w_o)}{w_o}}{\rho_l} \quad (5)$$

where w_s and w_0 are respective weight of the fully saturated and dry aerogel, respectively, and ρ_l is the liquid density (g/cm^3). The cyclic water and chloroform absorption of the aerogel (6.5 mg/cm^3) was measured by repetitive absorbing and squeezing out the liquids using a tweezers five times.

The densities (ρ) of the film were calculated from their mass and volume with a 14 μm measured thickness. The film was examined using a Leica DM2500 optical microscope equipped with a cross-polarizer. Water contact angles (WCAs) were measured on both top and bottom surfaces of each film by depositing 5 μL droplets of purified water, and the average of triplicate measurements on different areas was reported.

The root mean square (RMS) surface roughness of films was measured over a 10 μm x 10 μm area by AFM height image using Gwyddion software, and the average value from 3 images was reported. Nonpolar decane ($\varepsilon = 2.0$) with no dipole moment or H-bonding capability in comparison to $CHCl_3$ ($\varepsilon = 4.8$) was used to obtain the most contrasting to water wettability and absorption for the films. Water and decane absorption of aerogels and films were measured by percent mass gain from 3-second immersion in the liquid and lightly blotting excess surface liquid. Cyclic absorption of aerogels was conducted by squeezing with a tweezer following each absorption and repeated five times.

2.7. Re-dispersibility and thermal degradation pattern of fibers, films, and aerogels

The fibers, aerogels, and films were dispersed in liquids and sonicated (40 kHz, 130 W max, Branson ultrasonic processor model 2510) for one min to determine the extent of re-dispersibility. The fibers (10, 20, 60, and 120 mg) from varied CNF concentrations (0.05, 0.1, 0.3 w/v % and 0.6 w/v%) and the aerogel (30 mg) from 0.3 w/v% were immersed in 20 and 10 mL water, respectively. The film (30 mg) from 0.3 w/v% was immersed in 10 mL water, ethanol, and DMAc for 1 mo. and centrifuged at 5 k rpm for 15 min. The height of the re-dispersed CNFs (0.0005 w/v%) were observed by AFM. Thermal properties of AS cellulose, fibers, aerogels, and films (5 mg) were measured at 10 °C min^{-1} from 25 °C to 500 °C under purging N_2 (50 mL min^{-1}) using TGA-50 thermogravimetric analyzer (Shimadzu, Japan).

3. Results and discussion

3.1. AS cellulose isolation

Almond shell (AS) was separated from the fruits of soft-shell Carmel variety to consist 1:0.97:1.65 mass ratios of kernel/shell/hull. Cellulose was isolated from chestnut brown ground AS by three routes (Fig. 1). In Route 1, 2% mass was lost from 2:1 v/v toluene-ethanol extraction, another 18 % by acidified $NaClO_2$ oxidation, then 44.7 % by 5 % KOH treatment, yielding 35.3 % Cell 1. In Route 2, 17.2 % and 47.6 % mass were lost in respective $NaClO_2$ and KOH step, yielding 35.2 % Cell 2. White cellulose was produced in the same quantity by both Routes 1 and 2, suggesting the organic extraction to be unnecessary for isolating cellulose from AS. In Route 3, KOH and NaOH treatment removed similar mass of 34.4 % and 34.1 %, respectively, to brown colored products, evident of significant residual lignin, then $NaClO_2$ oxidized to only 26.6 % Cell 3, showing no advantage over Route 2. The overall mass balance from Routes 1 and 2 gave the AS compositions to be 2% organic extractables, 17.2–18 % lignin, 44.7–47.6 % hemicellulose, and 35.2–35.3 % cellulose.

Both Cell 1 and Cell 2 showed virtually identical FTIR with cellulose characteristic spectra that were absent of lignin aromatic skeletal vibrations at 1507 cm^{-1} and aromatic C=C-H bending at 818 cm^{-1} after $NaClO_2$ treatment, and hemicellulose at 1729 cm^{-1} for carbonyl stretching after KOH treatment (Fig. 2a, S1a). For Cell 3, the persisted lignin peaks at 1507 cm^{-1} after two consecutive alkaline treatment and a small carbonyl stretching shoulder at 1740 cm^{-1} following $NaClO_2$ treatment indicated possible oxidation of glucopyranose ring, showing Route 3 to be overly harsh (Fig. S1b). That Cell 2 not only had comparable yield but identical cellulose characteristic as Cell 1 confirms the organic extraction to be dispensable. Thus, the two step $NaClO_2$ (1.4%, pH 3–4, 70 °C, 5 h) and KOH (5%, rt, 24 h; 90 °C, 2 h) process or Route 2 is confirmed to be the optimal protocol for isolating cellulose from AS, producing 35.3% cellulose along with 17.2% lignin rich and 47.6% hemicellulose rich streams.

Cell 1 and Cell 2 showed virtually identical moisture contents (3.3, 3.5 %) while Cell 3 was slightly more hygroscopic (4.5 %), the latter being consistent with possible oxidation of glucopyranose rings. The T_{max} and char of Cell 1 were slightly higher than those of Cell 2 and Cell 3 (Fig. 2c), showing negligible effects of the minute non-cellulosics on their thermal behaviors. From the streamlined two step $NaClO_2$ and KOH process, this soft-shell variety AS contains more cellulose (35.3 %) but less organic extractable (2%) than those respective 28.9–32.6 % and 3.7–11.8 % values reported using standard methods (Table 1), further affirming organic extraction to be dispensable.

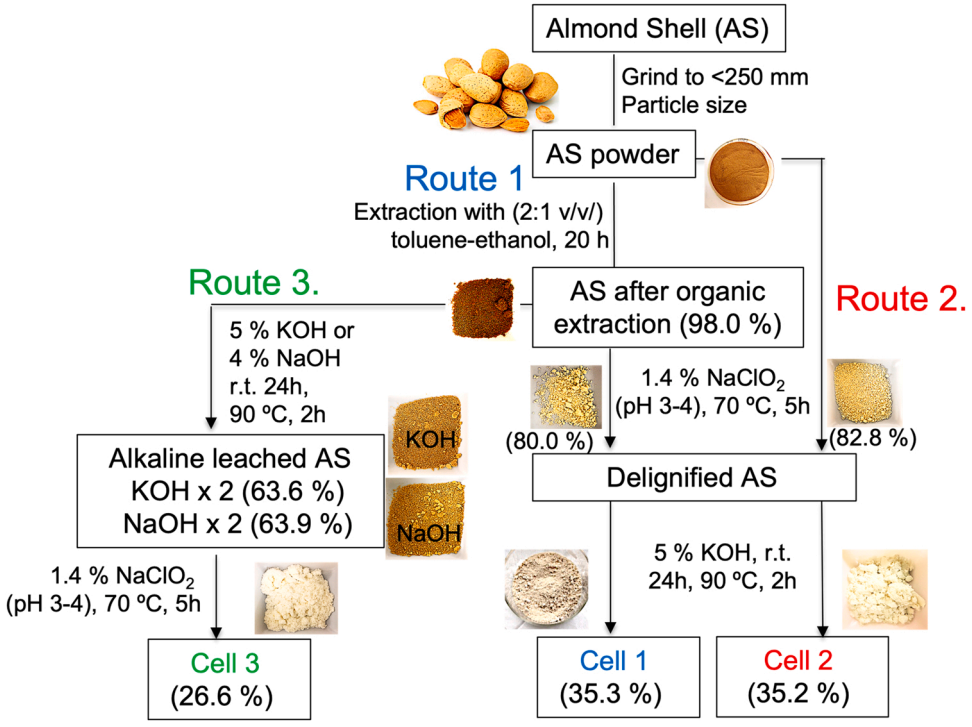

Fig. 1. Extraction flow chart for almond shell cellulose: Route 1, 2 and 3 for the three step, two step, and the reversed-order method.

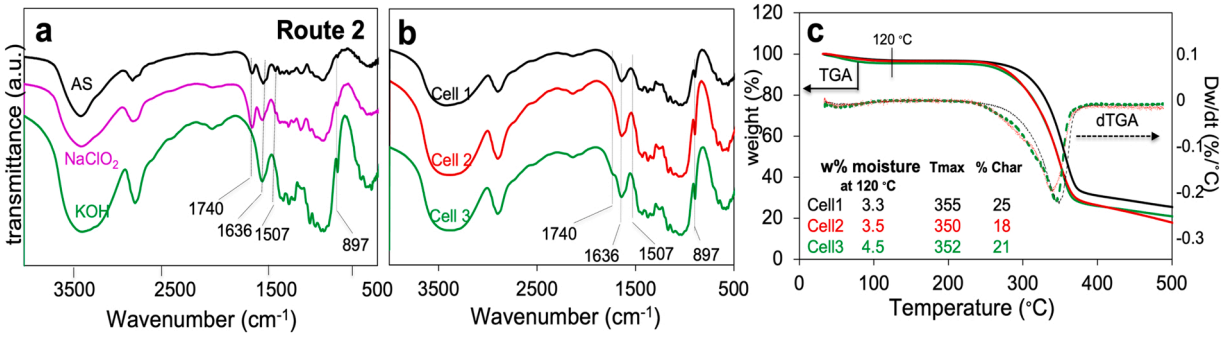

Fig. 2. Characteristics of isolated AS cellulose: (a) FTIR of isolates for Route 2; (b) FTIR and (c) TGA and *d*TGA of Cell 1, Cell 2, and Cell 3.

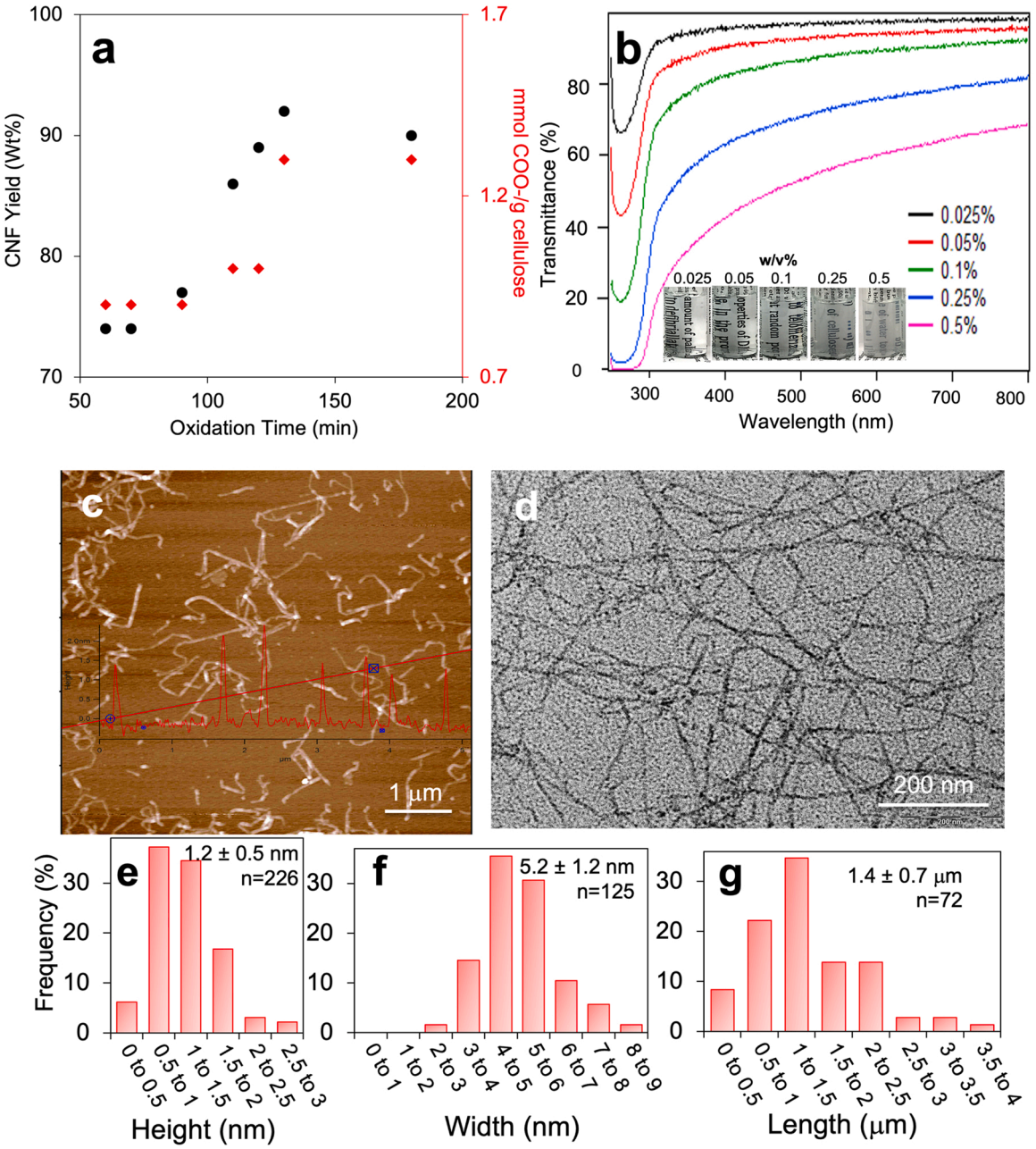

Fig. 3. Characteristics of CNF: (a) yield and charge density as a function of oxidation time; (b) UV–vis % transmittance and the photos showing clarity of the aqueous CNFs at varying concentrations. Morphology of CNF (1 mmol/g, 89 % yield): (c) AFM height image on mica; (d) TEM image on discharged carbon; corresponding (e) AFM based height; TEM based (f) width and (g) length distributions.

3.2. TEMPO-oxidized cellulose nanofibrils (CNFs)

The optimally isolated Cell 2 was TEMPO oxidized with 5 mmol NaClO primary oxidant per g of cellulose to regio-selectively transform the C6 primary hydroxyls to carboxyls. At pH 10, TEMPO oxidizes the cellulose OH in a five-membered transition state to accelerate the rate and pose a greater selectivity for primary C6 over the secondary C2 and C3 OH (Tojo and Fernández, 2007) (Fig. S2). High-speed blending of TEMPO oxidized cellulose produced an opaque aqueous slurry (c.a. 0.4 w/v%) that was centrifuged to collect the TEMPO-oxidized CNF

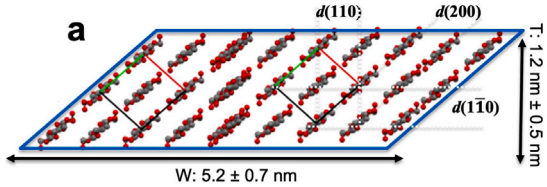

b

% COO^- per surface C6-OHs (%)	% COO^- per entire surface OHs (%)
60.7	20.2

$$\text{Surface C6-OHs} = \varphi_p = \frac{1}{2}\frac{N_s}{N_t} = \frac{\frac{w}{d(1\bar{1}0)}+1}{(\frac{T}{d(100)}+1)(\frac{w}{d(1\bar{1}0)}+1)} \quad \text{Eqn. 6}$$

$$\text{Where:} \quad Ns_p = 2\cdot\{(\frac{W}{d(1\bar{1}0)}+1)\} \quad \text{Eqn. 7}$$

$$Nt = \{\frac{T}{d(110)}+1\}\cdot\{\frac{W}{d(1\bar{1}0)}+1\} \quad \text{Eqn. 8}$$

$$\%\ \text{exposed C6-OH oxidized} = \frac{COO{-}charge}{total\ AGU\cdot\varphi} \quad \text{Eqn. 9}$$

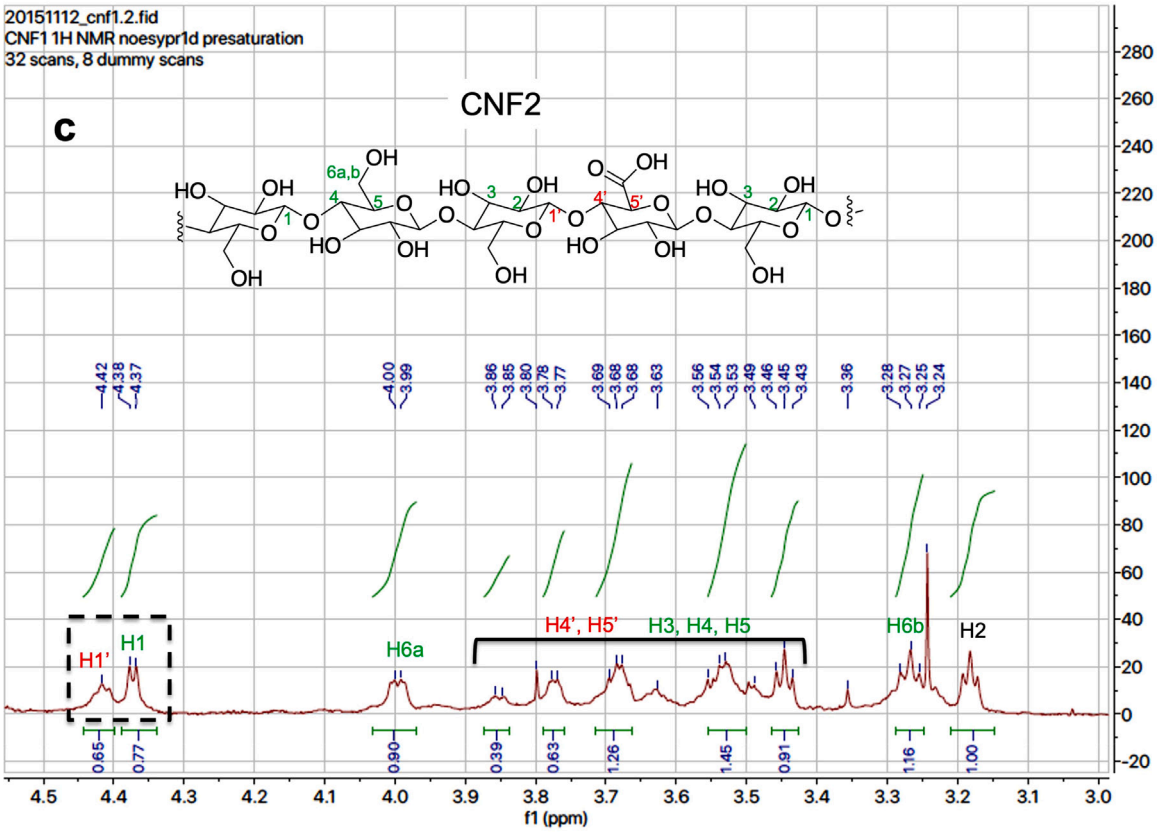

Fig. 4. Amphiphilic CNF surfaces: (a) parallelogram model representation of CNF crystalline cross-section with 110 lattice planes as W by TEM and 200 lattice plane as H by AFM; (b) percent COO^- per surface C6-OHs or all surface OHs; (c) HNMR of at c.a 0.0.02 w/v% CNF in D_2O.

supernatant. The conductometric titration of the sodium carboxylates of CNFs exhibited conductivity in a parabolic function with NaOH added (Fig. S3a). The initial steep decline corresponds to the neutralization of NaOH with the added HCl, followed by a plateau buffering region where both carboxylic acids and carboxylates were present, then the final incline as excess NaOH accumulated. While the CNF yields and the charge densities remained constant at 74–77 % and 0.9 mmol/g, respectively, from 60 to 90 min TEMPO reactions, both increased significantly to 86% and 1.0 mmol/g at 110 min, reaching the optimal 92 % yield and 1.30 mmol/g cell at 130 min (Fig. 3a). The duration of oxidation time for AS cellulose is similar to that for hardwood cellulose (Saito et al., 2007), both being of a woody source, but doubled that (1 h) for RS cellulose (Jiang and Hsieh, 2013), a cereal source, indicating slower oxidation or lower accessibility of TEMPO nitroxyl radicals in woody cellulose. The visible light transmittance of the aqueous CNF increased to > 90 % as concentration decreased to 0.025 %, showing little or no association among CNFs (Fig. 3b). Individual CNFs were ribbon-like and very long with average 1.2 ± 0.5 nm height (H), 5.2 ± 1.2 nm width (W), and 1.4 ± 0.7 μm length (L) from AFM and TEM (Fig. 3c-g), showing a ultra-high 1167 L/H aspect ratio and high 4.3 W/H cross-sectional anisotropy. It should be further noted that CNFs derived by the identical TEMPO and blending process from Cell 1 and Cell 3 had essentially the same H/W/L dimensions of 1.5 ± 0.8 nm/4.1 ± 1.2 nm/1.4 ± 0.6 μm and 1.0 ± 0.4 nm/4.4 ± 1.2 nm/1.2 ± 0.6 μm, respectively (Fig. S3b-k). In comparison, AS CNFs are similarly in height, but nearly 2.5 times wider and 40 % longer than rice straw CNFs with 1.5 nm/2.1 nm/1 μm H/W/L by the same TEMPO and blending process (Jiang and Hsieh, 2013).

3.3. Surface chemistry elucidated by a crystal structure model and ^{1}HNMR

To estimate the surface C6-OHs on CNFs, a simplified nanofibril cross-sectional model of parallelogram (Fig. 4a) was considered more probable over rectangle (Fig. S4) consistent with the previous evidence of shear force exposed 200 planes (Jiang and Hsieh, 2014). The width (W) and the height (H) values determined by AFM on hydrophilic mica and TEM on discharged carbon. D-spacings between 110, $1\bar{1}0$, and 200 lattice planes are 0.53 nm, 0.61 nm, and 0.39 nm, respectively. The parallelogram represents amphiphilic surfaces with hydrophilic 110 lattice planes exposed on the upper and lower surfaces and hydrophobic 200 along the two sides. In the parallelogram model, the number of surface anhydroglucose unite (AGU) chains (Ns_p) in the width direction are 2 x ($\frac{W}{d(1\bar{1}0)}+1$), to represent top and the bottom rows (Eq. 7), and the total number of AGU chains in the cross-section is given by Nt (Eq. 8). The C6-OHs are given by Ns_p divided by Nt multiplied by $\frac{1}{2}$ for one surface C6-OHs in every 2 AGUs (Eq. 6 or φ_p). Finally, the percentage of surface C6-OHs oxidized is presented by dividing the charge (mmol/g) by the total AGU (mol) multiplied by φ as in Eq. (9). This derivation gives an estimated 60.7 % conversion of the total surface C6-OHs to carboxylate groups, or 20.2 % COO^- of all surface OHs (Fig. 4b). The combination of double hydrogen bonding capacity of carboxylates and over 60 % surface C6-OH conversion to carboxylates significantly increased the polar-polar interaction of AS CNF surfaces through H-bonding. The strong polar-polar and H-bonding of the hydrophilic surfaces are further enhanced with the high 4.3 W/H cross-sectional anisotropy of AS CNF.

$$\text{Surface C6}-\text{OHs}=_p=\frac{1}{2}\frac{Ns}{Nt}=\frac{\frac{w}{d(1\bar{1}0)}+1}{\left(\frac{T}{d(100)}+1\right)\left(\frac{w}{d(1\bar{1}0)}+1\right)} \quad (6)$$

$$\text{Ns}_p=\left\{\left(\frac{W}{d(1\bar{0}0)}+1\right)\right\} \quad (7)$$

$$\text{Nt}=\left\{\frac{T}{d(110)}+1\right\}\left\{\frac{W}{d(1\bar{1}0)}+1\right\} \quad (8)$$

$$8\%\text{ exposed C6}-\text{OH oxidized}=\frac{COO-charge}{total\ AGU\cdot\varphi} \quad (9)$$

The surface protons on CNFs were measured by solution state ^{1}HNMR of never-dried aq. CNFs solvent exchanged via acetone to D_2O to prevent agglomeration (Fig. 4b). The furthest downfield peak at δ4.38 (H1) was assigned to the anomeric proton, consistent with δ4.41 (H1) chemical shift from rice straw CNFs (Jiang et al., 2014). The diastereotopic protons H6a,b appeared apart from each other at δ 4.00 and δ 3.27, also agreeing with the chemical shifts at δ 4.18 and δ 3.29 of rice straw CNF. H3, H4, and H5 protons at δ 3.45, δ 3.54 and δ 3.68 appeared as undefined multiplets, all consistent with respective protons at δ 3.52, δ 3.75 and δ 3.77 of rice straw CNFs. The slightly downfield peaks of H1′, H4′ and H5′ (δ 4.42, 3.63, 3.78) belong to oxidized glucuronic acids. They are more deshielded relative to H1, H4 and H5 on un-oxidized AGU, attributing to induction of electron-withdrawing carboxylate group moving electron density away from them. Those clear observable peaks of glucuronic acid protons demonstrated that the extent of surface carboxylate groups was reasonably high, agreeing with the parallelogram cross-sectional model.

3.4. Fibers

Freezing (−196 °C, 15 m) and freeze-drying of aq. CNFs (0.01–0.3 %) produced white featherlight fibrous mass (Fig. 5a-d insets), with those from lower concentrations (0.01–0.1 %) easily falling apart upon handling. The fibers from 0.01% aq. CNFs were 127 ± 72 nm wide while those from 0.05% were more than doubled in width of 278 ± 289 nm and more heterogeneous with some ribbon-like structure (Fig. 5e, f). Sub-micron thin film structure appeared at 0.1% then predominantly lamellar structure was observed at 0.3%. The self-assembling of CNFs into ca. 100–600 nm wide fibers and sub-micron thin films is attributed to minimal association of CNFs from rapid ice nucleation and localized crystallization by freezing at − 196 °C.

The XRD of the fibers from 0.1% CNFs and cellulose, both from Route 2, showed cellulose characteristic peaks at 2θ = 14.7°, 16.8° and 22.7° (Fig. 5g), corresponding to the $1\bar{1}0$, 110, and 200 crystallographic planes of the monoclinic cellulose I lattice, respectively. AS CNF had a 58.6% crystallinity and 2.54 nm crystallite size, preserving most (88% and 82% respectively) of original cellulose crystalline structure (66.4% and 3.1 nm, respectively). The 18% crystallite size reduction of AS CNF is less than the 35% reduction of RS CNFs from identical processes (Jiang and Hsieh, 2013) and may be attributed to their source difference, i.e., woody AS vs cereal RS.

3.5. 3.5. Aerogels

Aerogels were produced from freezing (−20 °C, 12 h) and freeze drying of the aqueous CNFs (0.05, 0.1, 0.3 and 0.6 w/v%) (Fig. 6a-d). Slower ice nucleation and large ice crystallization concentrated CNFs more to self-assemble extensively into film like structure at 0.05% (Fig. 6a) as opposed to fibers by rapid crystallization (Fig. 5b), then into predominantly inter-connecting thin-film structure at 0.1%, finally into the typical 3-D isotropic honey-comb porous aerogel structure with 200–300 μm cellular pore diameters at 0.3 % and 0.6% (Fig. 6c, d). The super low density (2.2–10.6 mg/mL) and the super high porosity (99.3–99.9 %) (Eq. 4) of AS aerogels were directly and inversely correlated with increasing CNF concentrations, respectively (Fig. 6e). All aerogels were amphiphilic, absorbing slightly more hydrophobic chloroform (74.8–121.0 mL/g) than water (47.6–127.3 mL/g) (Eq. 5) (Fig. 6f), except the 6.5 mg/cm^3 aerogel absorbing similarly, The binary polar and nonpolar affinity of the aerogel cellular wall surfaces is

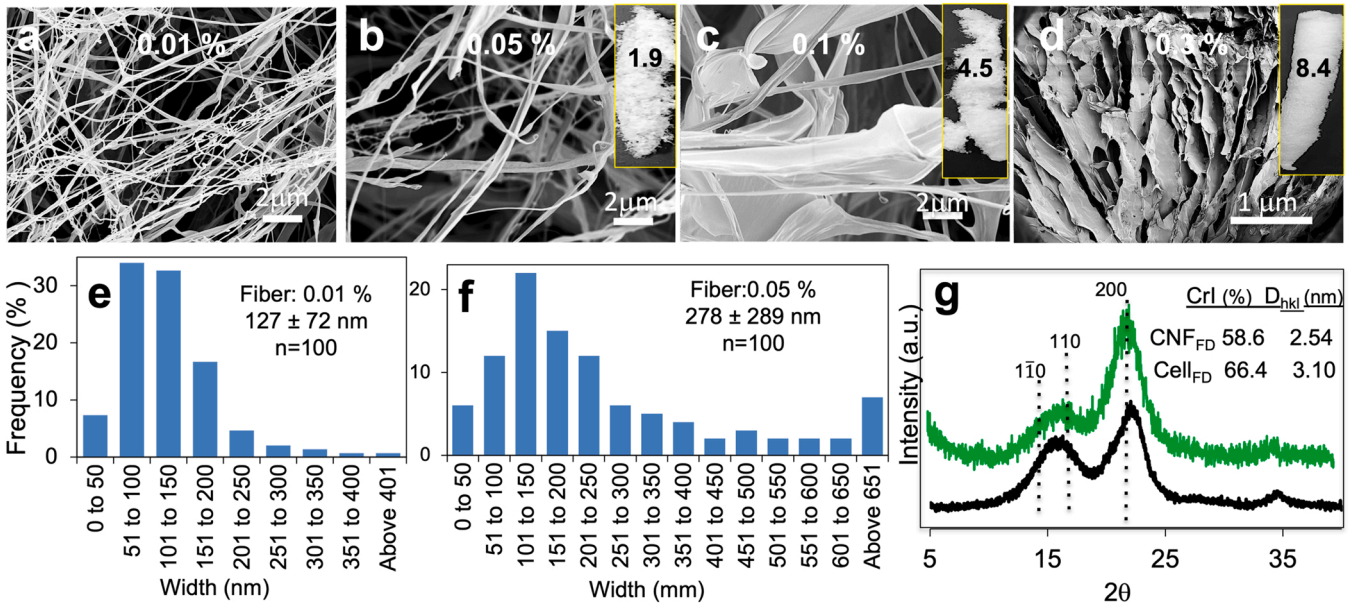

Fig. 5. Fibers: SEM images from initial concentrations of (a) 0.01 %; (b) 0.05 %; (c) 0.1 %; (d) 0.3 %; (e and f) width distributions of fibers from (a) and (b), respectively; (g) XRD of freeze-dried cellulose and fibers from 0.1 % CNF dispersions.

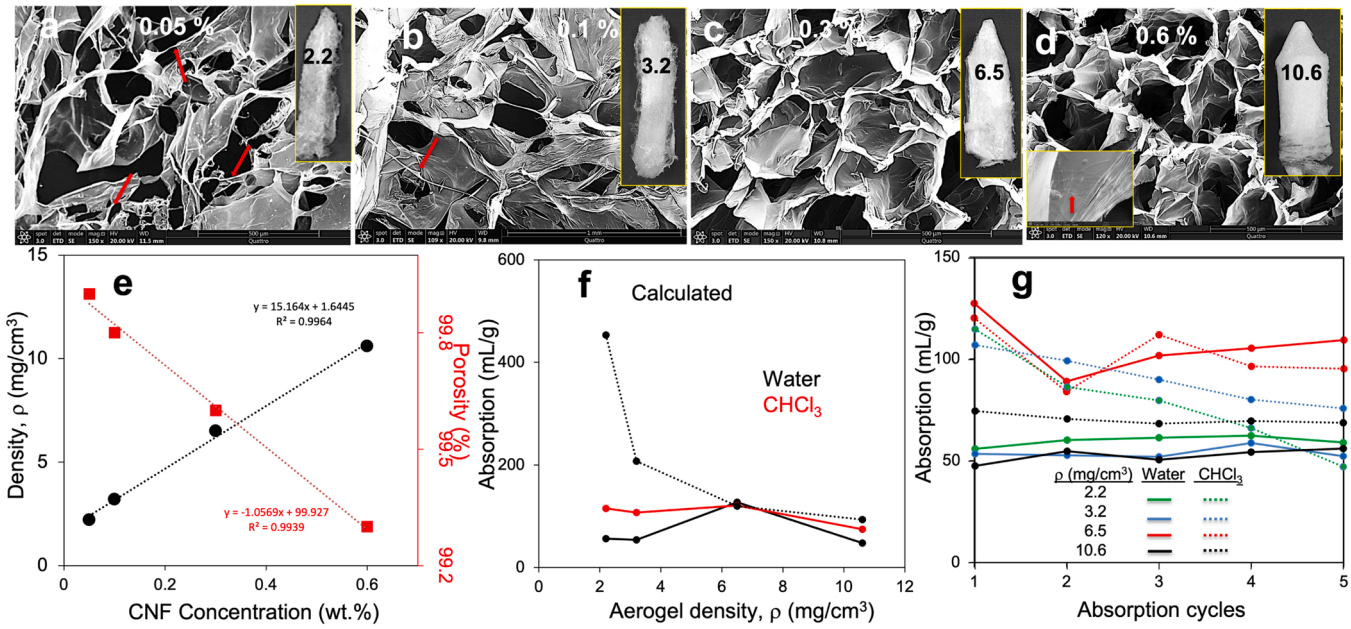

Fig. 6. Aerogels: SEM images of radial cross-sections from (a) 0.05 %; (b) 0.1 %; (c) 0.3 %; (d) 0.6 % CNFs. Inset photos are the corresponding aerogel samples. The red arrows indicate thin fibers; (e) density and porosity as a function of CNF concentration; (f) water and chloroform absorption with dashed line indicating absorption calculated from porosity; (g) cyclic water and chloroform absorption.(For interpretation of the references to colour in this figure, the reader is referred to the web version of this article.)

indicative of both polar-polar and nonpolar-nonpolar interfacial CNF associations via both hydrophilic (110) and hydrophobic (200) planes bringing forth the amphiphilic 3D porous structures. This amphiphilicity further support the CNF parallelogram crystalline model with both hydrophilic (110) and hydrophobic (200 planes (Fig. 4a). AS aerogel absorbed less water (120 mL/g) than RS aerogel (200 mL/g) formed at the same concentration of 0.3 w/v% and was attributed to its higher density (6.5 mg/cm^3 vs 4.0 mg/cm^3) or lower porosity.

All aerogels exhibited constant cyclic absorption and desorption of water up to five cycles except the 6.5 mg/cm^3 aerogel showing the highest initial water uptake then lowered in the following cycles, while still reabsorbed twice as much water as others (Fig. 6g). The less well-formed porous structures of lower density aerogels (2.2 and 3.2 mg/cm^3) absorbed over two times of chloroform than water, but chloroform absorption reduced continuously with subsequent cycles, consistent with less stable cellular wall structure from hydrophobic interaction. Even the decreasing cyclic chloroform absorption of aerogels with densities less than 6.5 mg/cm^3 had stable water absorption, showing impressive amphiphilic resiliency. Despite the lowest chloroform absorption, the densest aerogel (10.6 mg/cm^3) not only absorbed ca. 50% more chloroform than water but also exhibited consistent cyclic absorption of both liquids up to 5 cycles. Overall, the aerogels are

amphiphilic, absorbing ca. 25–50 % more hydrophobic chloroform than water, and highly absorbent of both at ca. 50 – 130 mL/g, and all water resilient to up to five cycles.

3.6. Films

The air-dried cast film from 3% aq. CNFs (90.6 mg) in PS trays were transparent, 14 μm thick, and 1.25 g/cm^3 in density (Fig. 7a), showing smoother top air-facing surface than the bottom PS-facing surface with respective roughness (RMS) of 30 ± 11 nm and 57 ± 24 nm (Fig. 7b, c), the latter likely due to the rough PS surface (RMS=1089 ± 14 nm) (Fig. S5). Optical microscopic images focusing on the top and the bottom surfaces showed the aligned microfibers (Fig. 7b, c), reflecting possibly respective marangoni and capillary flows of amphiphilic CNFs during drying. The internal bulk was porous (d = 94.1 ± 33.1 μm, n = 50, Fig. 7d) and slightly birefringent, evident of CNF association (Fig. 7d inset). The top surface was hydrophilic and had a water contact angle (WCA) of 34 ± 3° (Fig. 7b inset), same as reported for a cast cellulose film (Luner and Sandell, 1969), whereas the bottom surface had a slightly higher WCA of 43 ± 6 ° (Fig. 7c inset), again reflecting hydrophobic interaction with PS .

The films cast from increasing 0.1–0.6 % CNF concentrations had increasing densities of 0.99, 1.14, 1.25, to 1.36 g/cm^3, and decreasing porosity from 37 % to 15 % using 1.55 g/cm^3 for cellulose (Fig. 7d). All films exhibited some amphiphilicity, absorbing water close to the porosity but much less decane, indicative of the accessibility of internal pores to water (Fig. 7f). In fact, the porous cast film absorbed more than twice as much water (4.7 mL/g) as the more compacted vacuum-filtered film (1.8 mL/g) from rice straw CNF at the same 0.1 w/v% (Jiang and Hsieh, 2016). Water absorption significantly increased with increasing cycles from the initial 2.0, 3.3, 3.7 and 4.7 mL/g to 4.8, 5.6, 6.0 and 6.2 mL/g at the fifth cycle, increasing with densities, while the absorption of decane was only one third of water and varied little over five cycles (Fig. 7g). The significantly increased cyclic water absorption is consistent with more hydrophilic and water accessible bulk, and possibly swelling or expansion of internal pores, while the much lower and constant volume of decane absorbed is indicative of the less accessibility of decane into the seemly hydrophobic bulk and internal pores of the films.

3.7. Disassembling behaviors

Fibers, aerogels, and films were immersed in water and organic solvents and briefly sonicated to observe their disassembling behaviors. All fibrous mass from 0.05, 0.1, 0.3 and 0.6 w/v% were fully dispersed in water to CNFs in similar heights of 1.2 ± 0.6 nm, 1.2 ± 0.4 nm, 1.7 ± 0.7 nm, 1.1 ± 0.4 nm, respectively, as the original (Fig. 8a, S6, S7a), but ca. 10–20 % shorter, suggesting chain scissions by sonication. The fibers from 0.05 % and 0.1% dispersed readily and completely after 10–20 s sonication while those thin and lamellar films from 0.1 % and 0.3% (Fig. 5c, d) took three repetitive 10–20 s sonication with 5 s vortex in between, and those from 0.6 w/v% took 2–3 days to disintegrate. The complete re-dispersibility of the fibers in water supports the polar hydrophilic inter-CNF associations at low concentrations whereas the longer time to disperse those from higher concentrations suggests more abundant and/or stronger inter-CNF association and possibly entanglements. The rapid freezing process of assembling CNFs into fibers and their fast redispersibility back to individualized CNFs are advantageous for easier storage and transportation, re-dispersing and re-processing in and with other media and matrixes for more versatile formulation and applications.

The aerogel did not change appearance upon immersed in water for at least 3 d with daily vortex (3 s, 3x), then gradually dissociated into smaller pieces and viscous gel in another 7 d and remained as gel for the total of at least 10 d (Fig. S7b). The 10% supernatant from centrifugation (5000 rpm for 15 min) revealed mass of micro-gel structures interspersed with only few individual CNFs in similar height as the original (H:1.0–1.5 nm) (Fig. 8b, S8), but slightly shorter. The tenacious gel structure even in the supernatant after prolonged water immersion is consistent with the excellent water resiliency of the aerogel and supportive of the dominant hydrophobic association of CNFs in the cellular wall surfaces.

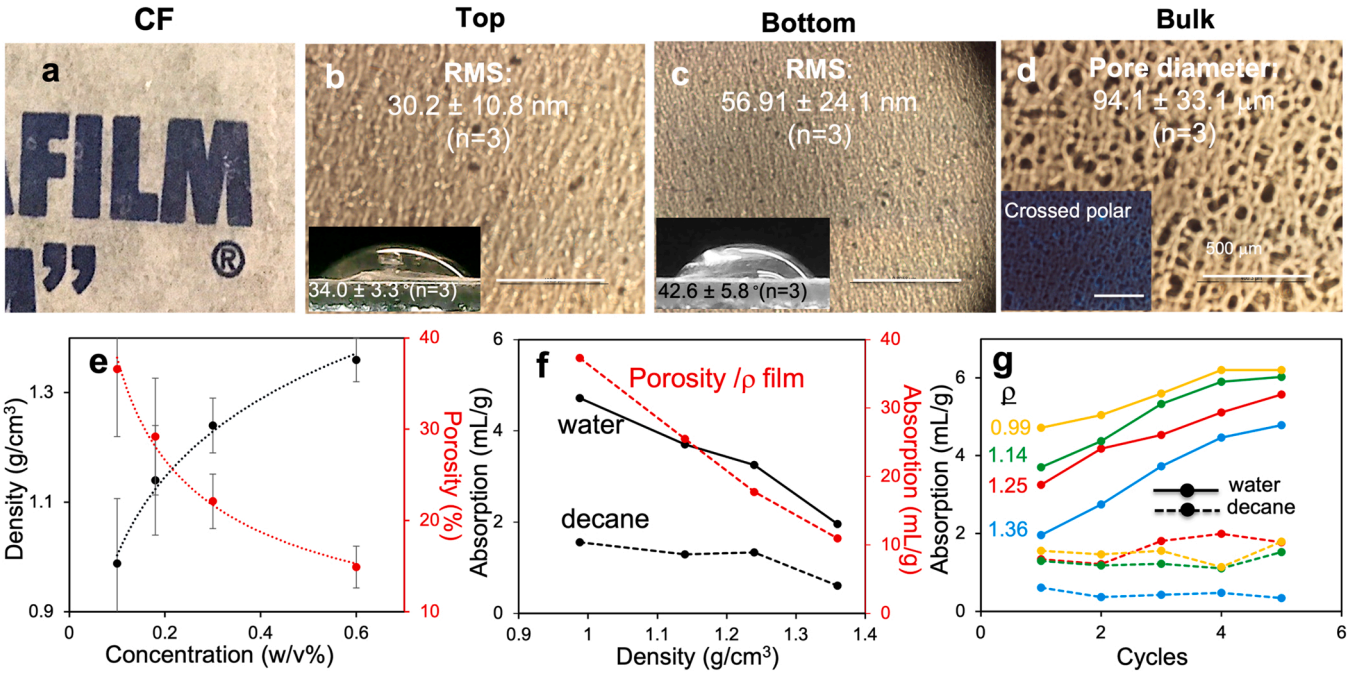

Fig. 7. Characteristics of films cast from aqueous CNF dispersions: (a) photographic image of a transparent film over a paper with a printed letter FILM; optical microscopic images (bar = 500 μm) focusing on (b) top and (c) bottom surfaces with corresponding WCA and RMS values; (d) internal bulk with the pore diameter, and the crossed-polar image in the inset; (e) the film density and the porosity as a function of dispersion concentration; (f) water and decane absorption with red dashed line indicating absorption calculated from porosity; (g) cyclic water and decane adsorption.

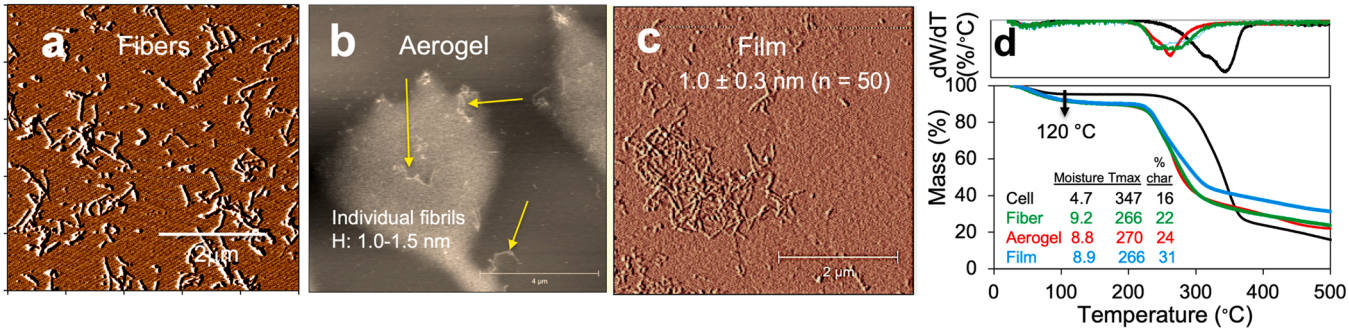

Fig. 8. Characteristics of fibers, aerogel, and films self-assembled from 0.3 w/v% CNF: (a) AFM of the supernatant from immediately 100 % redispersed fibers; (b) AFM of the supernatant from the redispersed aerogel at day 10; (c) AFM of the supernatant from the redispersed film at 3 mo. (d) TGA and dTGA.

The air-dried film disintegrated into small pieces in water in 2 days (Fig. S7c), but took three months with periodic vortex to re-disperse 71.7 % of the film (Fig. S8e) into CNFs with similar height (H: 1.0 ± 0.3 nm) (Fig. 8c) as the original (H: 1.2 ± 0.6 nm) while the rest 28.3 % remained as gel. In the less polar and far less H-bonding ethanol ($\delta p = 8.8$, $\delta h = 19.4$) and DMAc ($\delta p = 11.5$, $h = 10.2$) than water, ($\delta p = 16.0$, $\delta h = 42.3$), only 11.4 % and 7.5 % of the film was re-dispersible, respectively, without any CNFs but only submicron- or nano-size particles observed in the supernatants (Fig. S9b, c), giving little evidence of nonpolar-nonpolar inter-CNF association. While the film exhibited hydrophilic surfaces and amphiphilic bulk, absorbing more water than decane (Fig. 7g), the much reduced redispersibility in water and even less in the less polar ethanol and DMAc supports the dominant polar inter-CNF associations in the air-drying process.

Overall, AS-CNFs self-assembled into fibers, aerogels , and films via both hydrophilic and hydrophobic surface associations, but to different degrees and influenced by the solidification conditions. While both films and aerogels are amphiphilic, aerogels are super-absorbents, absorbing more hydrophobic liquids, whereas films are hydrophilic on the surface and absorb more water than non-polar decane, in particular with increasing cycles. The descending water redispersibility of fibers, aerogels, and films supports the increasing and more abundant inter-CNF associations via hydrophobic non-polar and/or stronger H-bonding. The moisture contents in the fibers, aerogels, and films were similar (9.2 %, 8.8 % and 8.9 % respectively), nearly double of cellulose (4.7 %). The respective T_{max} (266, 270 and 266 °C respectively) were close to each other but significantly lower than that of cellulose (347 °C) (Fig. 8d). Both higher moisture contents and lowered T_{max} of AS CNF solids are expected from oxidation and nano-scale lateral dimensions, also observed on RS CNF (Jiang and Hsieh, 2013). Higher chars from fibers, aerogels, and films (22 %, 24 %, and 31 %, respectively) than cellulose (16 %) are supportive of enhanced interfacial CNF associations. The highest chars from films may indicate their particularly strong and recalcitrant characteristics, consistent with their least redispersibility in water as well as in non-polar decane. The amphiphilic and water resilient aerogels and organic liquid resilient films are attributed largely to the particularly strong interfacial associations of AS CNF driven by their uniquely cross-sectional anisotropy and proportionally high 4.3 hydrophilic surfaces, promising as absorbents, membranes, and nanopapers.

4. Conclusion

This is the first comprehensive study on efficient cellulose isolation and optimized cellulose nanofibril (CNF) generation from almond shell (AS) and their self-assembling into solid structural materials. The soft-shell Carmel variety consisted of nearly equal mass of AS as kernel in 1:0.97:1.65 kernel/shell/hull mass ratio. Over 35 % cellulose was isolated from AS by a streamlined two-step oxidation-alkali protocol, i.e., $NaClO_2$ (1.4 %, pH 3–4, 70 °C, 5 h) and KOH (5 %, rt, 24 h 90 °C, 2 h), along with up to 18% lignin, 47 % hemicellulose, and negligible organic extractables. AS-CNFs have been generated in up to 92% yield from coupled TEMPO-mediation oxidation and high-speed blending to have average 1.2 nm height (H), 5.2 nm width (W), 1.4 μm length, 58.6 % crystallinity, and 1.3 mmole/g charge. The uniquely super-high L/H aspect ratio and anisotropic W/H lateral dimension or 1167/4.3/1 (L/W/H) of AS-CNF, are modeled by a parallelogram cross-section to give estimated 61 % conversion of surface C6-OH to carboxylate, or 20 % conversion of all surface OHs, supported by ^{1}HNMR. Aq. CNFs were self-assembled into 1D fibers and 3D aerogels by freezing at − 196 °C and − 20 °C, respectively, then lyophilization as well as 2D cast films by air drying. The aq. to solid transformation induces interfacial CNF associations via both hydrophilic polar-polar interactions between the 110 planes and hydrophobic nonpolar-nonpolar between the 200 lattice planes, but to different degrees. The fibers could be fully re-dispersed to individualized CNFs, advantageous for easier storage and transportation, re-dispersing and re-processing in and with diverse media and matrixes for versatile formulation and applications. The aerogels are amphiphilic super-absorbents, absorbing slightly more hydrophobic chloroform (75–121 mL/g) than water (48–128 mL/g), whereas the films are hydrophilic on the surface and internally, absorbing more water (2.0–4.7 mL/g) than nonpolar decane (0.5–1.1 mL/g) and increasing water absorption with increasing cycles. The highly anisotropic AS CNFs and their self-assembling into 1D, 2D, and 3D materials with unique dispersing dispersive behaviors, amphiphilicities, wet resiliency demonstrated great potentials as aq. and organic dispersible CNFs, amphiphilic absorbents, gels, and films, aq. and organic resilient membranes and nanopapers.

CRediT authorship contribution statement

Juri Fukuda: Experimental Execution, Data analyses, Presentation, Writing – original draft, Revision. **You-Lo Hsieh:** Conceptualization, Funding acquisition, Review, Writing revision.

Declaration of Competing Interest

The authors declare that they have no known competing financial interests or personal relationships that could have appeared to influence the work reported in this paper.

Acknowledgement

USDA Western Sun Grant Program and Henry A. Jastro Research Award, University of California, Davis are greatly appreciated.

Notes

The authors declare no competing financial interest.

Appendix A. Supporting information

Supplementary data associated with this article can be found in the online version at doi:10.1016/j.indcrop.2022.115188.

References

Almond Board of California, 2020 Almond Almanac. ⟨https://www.almonds.com/sites/default/files/2020–12/2020%20Almond%20Almanac.pdf⟩.

Chiou, B.-S., Valenzuela-Medina, D., Bilbao-Sainz, C., Klamczynski, A.P., Avena-Bustillos, R.J., Milczarek, R.R., Du, W.-X., Glenn, G.M., Orts, W.J., 2016. Torrefaction of almond shells: Effects of torrefaction conditions on properties of solid and condensate products. Ind. Crops Prod. 86, 40–48. https://doi.org/10.1016/j.indcrop.2016.03.030.

Chiou, B.-S., Valenzuela-Medina, D., Wechsler, M., Bilbao-Sainz, C., Klamczynski, A.K., Williams, T.G., Wood, D.F., Glenn, G.M., Orts, W.J., 2015. Torrefied biomass-polypropylene composites. J. Appl. Polym. Sci. 132. https://doi.org/10.1002/app.41582.

De Bari, I., Barisano, D., Cardinale, M., Matera, D., Nanna, F., Viggiano, D., 2000. Air gasification of biomass in a downdraft fixed bed: a comparative study of the inorganic and organic products distribution. Energy Fuels 14, 889–898. https://doi.org/10.1021/ef990243g.

El Mechtali, F.Z., Essabir, H., Nekhlaoui, S., Bensalah, M.O., Jawaid, M., Bouhfid, R., Qaiss, A., 2015. Mechanical and thermal properties of polypropylene reinforced with almond shells particles: impact of chemical treatments. J. Bionic Eng. 12, 483–494. https://doi.org/10.1016/S1672-6529(14)60139-6.

Estevinho, B.N., Ratola, N., Alves, A., Santos, L., 2006. Pentachlorophenol removal from aqueous matrices by sorption with almond shell residues. J. Hazard. Mater. 137, 1175–1181. https://doi.org/10.1016/j.jhazmat.2006.04.001.

Fukuzumi, H., Saito, T., Iwata, T., Kumamoto, Y., Isogai, A., 2009. Transparent and high gas barrier films of cellulose nanofibers prepared by TEMPO-mediated oxidation. Biomacromolecules 10, 162–165. https://doi.org/10.1021/bm801065u.

García, R., Pizarro, C., Lavín, A.G., Bueno, J.L., 2017. Biomass sources for thermal conversion. Techno-economical overview. Fuel 195, 182–189. https://doi.org/10.1016/j.fuel.2017.01.063.

Gong, D., Holtman, K.M., Franqui-Espiet, D., Orts, W.J., Zhao, R., 2011. Development of an integrated pretreatment fractionation process for fermentable sugars and lignin: application to almond (Prunus dulcis) shell. Biomass Bioenergy 35, 4435–4441. https://doi.org/10.1016/j.biombioe.2011.08.022.

González, J.F., Ramiro, A., González-García, C.M., Gañán, J., Encinar, J.M., Sabio, E., Rubiales, J., 2005. Pyrolysis of almond shells. Energy applications of fractions. Ind. Eng. Chem. Res. 44, 3003–3012. https://doi.org/10.1021/ie0490942.

Hashemian, S., 2014. A comparative study of cellulose agricultural wastes (almond shell, pistachio shell, walnut shell, tea waste and orange peel) for adsorption of violet B dye from aqueous solutions. Orient J. Chem. 30, 2091–2098. https://doi.org/10.13005/ojc/300478.

Huang, G.and Lapsley, K., 2019. Chapter 15 Almond in Integrated Processing Technologies for Food and Agricultural By-Products, edited by Pan, Z.; Zhang, R.; Zicari, S.; Academic Press.

, 2020International Treenuts and Dried Fruits Council (INC), Statistical Yearbook 2020/2021.https://www.nutfruit.org/industry/news/detail/statistical-yearbook (Accessed 2021 -07 -25).

Iwamoto, S., Kai, W., Isogai, A., Iwata, T., 2009. Elastic modulus of single cellulose microfibrils from tunicate measured by atomic force microscopy. Biomacromolecules 10, 2571–2576. https://doi.org/10.1021/bm900520n.

Izquierdo, M.T., Martínez de Yuso, A., Rubio, B., Pino, M.R., 2011. Conversion of almond shell to activated carbons: methodical study of the chemical activation based on an experimental design and relationship with their characteristics. Biomass Bioenergy 35, 1235–1244. https://doi.org/10.1016/j.biombioe.2010.12.016.

Jiang, F., Dallas, Jerry, L., Ahn, B.K., Hsieh, Y.-L., 2014. 1D and ^{2}D NMR of nanocellulose in aqueous colloidal suspensions. Carbohydr. Polym. 110, 360–366. https://doi.org/10.1016/j.carbpol.2014.03.043.

Jiang, F., Han, S., Hsieh, Y.-L., 2013. Controlled defibrillation of rice straw cellulose and self-assembly of cellulose nanofibrils into highly crystalline fibrous materials. RSC Adv. 3, 12366–12375. https://doi.org/10.1039/c3ra41646a.

Jiang, F., Hsieh, Y.-L., 2013. Chemically and mechanically isolated nanocellulose and their self-assembled structures. Carbohydr. Polym. 95, 32–40. https://doi.org/10.1016/j.carbpol.2013.02.022.

Jiang, F., Hsieh, Y.-L., 2014. Amphiphilic superabsorbent cellulose nanofibril aerogels. J. Mater. Chem. A 2, 6337–6342. https://doi.org/10.1039/c4ta00743c.

Jiang, F., Hsieh, Y.-L., 2016. Self-assembling of TEMPO oxidized cellulose nanofibrils as affected by protonation of surface carboxyls and drying methods. ACS Sustain. Chem. Eng. 4, 1041–1049. https://doi.org/10.1021/acssuschemeng.5b01123.

Kacem, I., Koubaa, M., Maktouf, S., Chaari, F., Najar, T., Chaabouni, M., Ettis, N., Ellouz Chaabouni, S., 2016. Multistage process for the production of bioethanol from almond shell. Bioresour. Technol. 211, 154–163. https://doi.org/10.1016/j.biortech.2016.03.057.

Kamali-Gharamaleki, M., Sadeghi, B., Rouhani, M., Mirjafary, Z., 2021. Preparation and characterization of novel nano-cellulose-OSO3H prepared from the almond shell as a catalyst and its application in synthesis of 2-amino-3-phenylsulfonyl-4-Aryl-4H-benzo[h]chromen derivatives. Polycycl. Aromat. Compd. 0, 1–13. https://doi.org/10.1080/10406638.2021.1984261.

Klasson, K.T., Uchimiya, M., Lima, I.M., 2015. Characterization of narrow micropores in almond shell biochars by nitrogen, carbon dioxide, and hydrogen adsorption. Ind. Crops Prod. 67, 33–40. https://doi.org/10.1016/j.indcrop.2015.01.010.

Lu, P., Hsieh, Y.-L., 2012. Preparation and characterization of cellulose nanocrystals from rice straw. Carbohydr. Polym. 87, 564–573. https://doi.org/10.1016/j.carbpol.2011.08.022.

Luner, P., Sandell, M., 1969. The wetting of cellulose and wood hemicelluloses. J. Polym. Sci. Part C Polym. Symp. 28, 115–142. https://doi.org/10.1002/polc.5070280112.

Maaloul, N., Arfi, R.B., Rendueles, M., Ghorbal, A., Diaz, M., 2017a. Dialysis-free extraction and characterization of cellulose crystals from almond (Prunus dulcis) shells 8, 11.

Maaloul, N., Oulego, P., Rendueles, M., Ghorbal, A., Díaz, M., 2017b. Novel biosorbents from almond shells: characterization and adsorption properties modeling for Cu(II) ions from aqueous solutions. J. Environ. Chem. Eng. 5, 2944–2954. https://doi.org/10.1016/j.jece.2017.05.037.

Martínez de Yuso, A., Rubio, B., Izquierdo, M.T., 2014. Influence of activation atmosphere used in the chemical activation of almond shell on the characteristics and adsorption performance of activated carbons. Fuel Process. Technol. 119, 74–80. https://doi.org/10.1016/j.fuproc.2013.10.024.

Martínez, J.M., Reguant, J., Montero, M.Á., Montané, D., Salvadó, J., Farriol, X., 1997. Hydrolytic pretreatment of softwood and almond shells. degree of polymerization and enzymatic digestibility of the cellulose fraction. Ind. Eng. Chem. Res. 36, 688–696. https://doi.org/10.1021/ie960048e.

Mehrasbi, M.R., Farahmandkia, Z., Taghibeigloo, B., Taromi, A., 2009. Adsorption of lead and cadmium from aqueous solution by using almond shells. Water Air Soil Pollut. 199, 343–351. https://doi.org/10.1007/s11270-008-9883-9.

Messa, L.L., Faez, R., Hsieh, Y.-L., 2021. Phosphorylated cellulose nanofibrils from sugarcane bagasse with pH tunable gelation. Carbohydr. Polym. Technol. Appl. 2, 100085 https://doi.org/10.1016/j.carpta.2021.100085.

Nabais, J.M.V., Laginhas, C.E.C., Carrott, P.J.M., Ribeiro Carrott, M.M.L., 2011. Production of activated carbons from almond shell. Fuel Process. Technol., III Int. Congr. Energ. Eng. Environ. 92, 234–240. https://doi.org/10.1016/j.fuproc.2010.03.024.

Nabarlatz, D., Torras, C., Garcia-Valls, R., Montané, D., 2007. Purification of xylo-oligosaccharides from almond shells by ultrafiltration. Sep. Purif. Technol. 53, 235–243. https://doi.org/10.1016/j.seppur.2006.07.006.

Nepomuceno, N.C., Santos, A.S.F., Oliveira, J.E., Glenn, G.M., Medeiros, E.S., 2017. Extraction and characterization of cellulose nanowhiskers from Mandacaru (Cereus jamacaru DC.) spines. Cellulose 24, 119–129. https://doi.org/10.1007/s10570-016-1109-5.

Pirayesh, H., Khazaeian, A., 2012. Using almond (Prunus amygdalus L.) shell as a bio-waste resource in wood based composite. Compos. Part B Eng. 43, 1475–1479. https://doi.org/10.1016/j.compositesb.2011.06.008.

Queirós, C.S.G.P., Cardoso, S., Lourenço, A., Ferreira, J., Miranda, I., Lourenço, M.J.V., Pereira, H., 2020. Characterization of walnut, almond, and pine nut shells regarding chemical composition and extract composition. Biomass Conv. Bioref. 10, 175–188. https://doi.org/10.1007/s13399-019-00424-2.

Rashid, S., Shahi, A.K., Dutta, H., Sahu, J.K., 2022. Extraction and characterization of cellulose and cellulose nanowhiskers from almond shell biomass, metal removal and toxicity analysis. Biointerface Res. Appl. Chem. 12, 1705–1720. https://doi.org/10.33263/BRIAC122.17051720.

Sabbatini, A., Lanari, S., Santulli, C., Pettinari, C., 2017. Use of almond shells and rice husk as fillers of poly(Methyl Methacrylate) (PMMA) composites. Materials 10, 872. https://doi.org/10.3390/ma10080872.

Saito, T., Kimura, S., Nishiyama, Y., Isogai, A., 2007. Cellulose nanofibers prepared by TEMPO-mediated oxidation of native cellulose. Biomacromolecules 8, 2485–2491. https://doi.org/10.1021/bm0703970.

Saura-Calixto, F., Canellas, J., Garcia-Raso, J., 1983. Contents of detergent-extracted dietary fibers and composition of hulls, sheels, and teguments of almonds (Prunus amygdalus). J. Agric. Food Chem. 31, 1255–1259. https://doi.org/10.1021/jf00120a027.

Scherrer, P, 1918. Estimation of the size and internal structure of 917 colloidal particles by means of Röntgen rays. Nachr. Ges. Wiss. Göttingen 2, 96–100.

Segal, L., Creely, J.J., Martin, A.E., Conrad, C.M., 1959. An empirical method for estimating the degree of crystallinity of native cellulose using the X-ray diffractometer. Text. Res. J. 29, 786–794. https://doi.org/10.1177/004051755902901003.

Sun, J.X., Sun, X.F., Zhao, H., Sun, R.C., 2004. Isolation and characterization of cellulose from sugarcane bagasse. Polym. Degrad. Stab. 84, 331–339. https://doi.org/10.1016/j.polymdegradstab.2004.02.008.

Thomas Klasson, K., Ledbetter, Craig, A., Wartelle, L.H., Lingle, S.E., 2010. Feasibility of dibromochloropropane (DBCP) and trichloroethylene (TCE) adsorption onto activated carbons made from nut shells of different almond varieties. Ind. Crops Prod. 31, 261–265. https://doi.org/10.1016/j.indcrop.2009.11.002.

Tojo, G., Fernández, M., 2007. TEMPO-Mediated Oxidations, in: Tojo, G., Fernández, M. (Eds.), Oxidation of Primary Alcohols to Carboxylic Acids: A Guide to Current Common Practice, Basic Reactions in Organic Synthesis. Springer, New York, NY, pp. 79–103. https://doi.org/10.1007/0–387-35432–8_6.

Urruzola, I., Robles, E., Serrano, L., Labidi, J., 2014. Nanopaper from almond (Prunus dulcis) shell. Cellulose 21, 1619–1629. https://doi.org/10.1007/s10570-014-0238-y.

Wu, X., Moon, R.J., Martini, A., 2014. Tensile strength of Iβ crystalline cellulose predicted by molecular dynamics simulation. Cellulose 21, 2233–2245. https://doi.org/10.1007/s10570-014-0325-0.

Yousefi, H., Faezipour, M., Hedjazi, S., Mousavi, M.M., Azusa, Y., Heidari, A.H., 2013. Comparative study of paper and nanopaper properties prepared from bacterial

cellulose nanofibers and fibers/ground cellulose nanofibers of canola straw. Ind. Crops Prod. 43, 732–737. https://doi.org/10.1016/j.indcrop.2012.08.030.